

IMPROVED METHOD TO DETERMINE THE INTEGRATED PROPERTIES OF NUCLEAR RINGS: NGC 1512

CHAO MA¹, RICHARD DE GRIJS^{1,2}, AND LUIS C. HO¹

Accepted for publication in The Astrophysical Journal Supplements

ABSTRACT

The integrated properties of nuclear rings are correlated with their host galaxy’s secular evolution and its dynamics, as well as with the formation and evolution of the ring’s star cluster population(s). Here we present a new method to accurately measure the spectral energy distribution and current star-formation rate (SFR) of the nuclear ring in the barred spiral galaxy NGC 1512 based on high-resolution *Hubble* and *Spitzer Space Telescope* images. Image degradation does not have a significant negative effect on the robustness of the results. To obtain the ring’s SFR for the period spanning $\sim 3\text{--}10$ Myr, we apply our method to the continuum-subtracted $H\alpha$ and $8\ \mu\text{m}$ images. The resulting SFR surface density, $\Sigma_{\text{SFR}} = 0.09\ M_{\odot}\ \text{yr}^{-1}\ \text{kpc}^{-2}$, which is much higher than the disk-averaged SFR densities in normal galaxies. We also estimate the ring’s total stellar mass, $\log(M/M_{\odot}) = 7.1 \pm 0.11$ for an average age of ~ 40 Myr.

Subject headings: methods: observational – galaxies: evolution – galaxies: individual (NGC 1512) – galaxies: fundamental parameters – galaxies: star formation

1. INTRODUCTION

Circumnuclear starburst rings, which are usually found within 1 kpc of galactic nuclei, are interesting substructures that are often subject to intense starbursts. They are mostly found in barred spiral galaxies, since they are the natural products of bar-induced dynamics, although it has been reported that merger events and other non-axisymmetric structures—such as oval/elliptically shaped density enhancements and strong spiral arms—in some unbarred galaxies can also generate nuclear rings (e.g., NGC 7217 and NGC 7742; Shlosman et al. 1990; Athanassoula 1994; Combes 2001; Kormendy & Kennicutt 2004; Mazzuca et al. 2006; Sil’chenko & Moiseev 2006). The gravitational torque from the asymmetric bar potential causes gas infall toward the nucleus along the dust lanes at the leading edges of the bar (e.g., Byrd et al. 1994; Knapen et al. 1995; Regan & Teuben 2003; Kim et al. 2012a). The inflowing materials, which lose most of their angular momentum, spiral in toward the ring region at the two ‘contact points’ between the dust lanes and the ring, where the accumulated gas proceeds to move in nearly circular orbits and forms a luminous, compact ring around the galactic center (e.g., Athanassoula 1992; Buta & Combes 1996; Maciejewski 2004; Kim et al. 2012b).

The high gas density (e.g., Wild et al. 1992; Mazzuca et al. 2008; Comerón et al. 2010), the unusually short crossing timescale, and the enhanced collision rate in the ring may consequently trigger violent starburst episodes, which often dominate the entire star-formation history of the host galaxy (e.g., Genzel et al. 1995; Knapen et al. 2006; Mazzuca et al. 2011). Comprehensive studies of nuclear rings are therefore paramount to understand the secular evolution and dynamics of spiral galaxies. Over the course of several

decades, many theoretical and observational studies have contributed significantly to our knowledge of nuclear ring properties (e.g., Burbidge & Burbidge 1960; Sandage 1961; Hummel et al. 1987; Buta & Crocker 1993; Englmaier & Shlosman 2000; van der Laan et al. 2013). Owing to the close connection between rapid star formation and the presence of young star clusters, nuclear rings are prime regions in nearby disk galaxies where young massive star clusters are found in abundance (e.g., Barth et al. 1995; Maoz et al. 1996; Hsieh et al. 2012; de Grijs & Anders 2012; van der Laan et al. 2013; de Grijs et al. 2017).

The properties of nuclear rings are also good diagnostics to constrain the host galaxy’s structural parameters (e.g., Weiner et al. 2001; Kormendy & Kennicutt 2004; Li et al. 2015). They thus serve as important features connecting galaxy-scale properties to the star cluster population. Since our ultimate purpose is to explore how the ring environment (or the integrated ring properties) affects the evolution of the young cluster population, it is of great importance to derive the integrated ring parameters, such as their total luminosities and their star-formation rates (SFRs). Traditional approaches to calculate the global ring SFR (e.g., Buta et al. 1999; Maoz et al. 2001; Mazzuca et al. 2008) usually follow Kennicutt (1998):

$$\text{SFR}\ (M_{\odot}\ \text{yr}^{-1}) = 7.9 \times 10^{-42} [L(H\alpha)_{\text{obs}}], \quad (1)$$

where $L(H\alpha)_{\text{obs}}$ represents the $H\alpha$ emission-line luminosity, which is usually directly derived from the imaging. However, as readily recognized by these authors, application of this equation could result in large uncertainties of up to 50% (e.g., Kennicutt 1998) because of the presence of variable extinction across the ring, although some investigators have tried to minimize this effect by adopting a representative ring cluster extinction value (e.g., Buta et al. 2000; Benedict et al. 2002). To circumvent the dust-attenuation problem, it is indispensable to combine observations of ultraviolet or optical SFR tracers with complementary infrared measurements so as to

¹ Kavli Institute for Astronomy & Astrophysics and Department of Astronomy, Peking University, Yi He Yuan Lu 5, Hai Dian District, Beijing 100871, China; machao@pku.edu.cn

² International Space Science Institute–Beijing, 1 Nanertiao, Zhongguancun, Hai Dian District, Beijing 100190, China

account for missing flux caused by the dust absorption and scattering (for a review, see e.g. Kennicutt & Evans 2012, and references therein).

Mazzuca et al. (2008) have shown that nuclear rings are coplanar with their disks and retain nearly circular shapes after deprojection. Since these structures are embedded in the galactic disk and bulge of their host galaxy, the total, intrinsic ring luminosities measured are unavoidably contaminated by contributions from the host galaxy. However, few studies have taken background corrections into account when calculating the total ring flux, except for Maoz et al. (1996), who measured the total ring flux by integrating all counts above the background over the entire ring region. Note that their background measure is, in fact, a constant value, determined in an ‘empty’ corner of the image. This thus only provides a simple approximation to the often highly complex background in the ring region. Consequently, the main motivation for this paper is to demonstrate the feasibility of a newly devised method to obtain clean ring luminosities based on galaxy light-profile fitting using the GALFIT algorithm (Peng et al. 2002, 2010).

As a test case, we will obtain the spectral energy distribution (SED) and SFR of the luminous nuclear ring in the galaxy NGC 1512, while simultaneously allowing for inherent dust attenuation and background correction. Our analysis is based on multi-waveband *Hubble Space Telescope* (*HST*) imaging data, combined with observations obtained with the Infrared Array Camera (IRAC) on board the *Spitzer* Space Telescope. NGC 1512 is located at high Galactic latitude and it is, hence, barely affected by Galactic foreground extinction, $E(B - V) = 0.011$ mag (Schlegel et al. 1998); we will hence ignore any correction for Galactic foreground reddening. The remainder of this paper is organized as follows. In Section 2, we describe the observational data used as well as our data reduction approach. Section 3 presents in detail our improved procedure for calculating the ring flux, and addresses a series of technical issues. Finally, we provide a brief summary and our main conclusions in Section 4.

2. OBSERVATIONS AND DATA REDUCTION

Broad-band *HST*/Wide Field Camera-3 (WFC3; pixel size $\sim 0.04''$) images of NGC 1512 were acquired from the *HST* Legacy Archive (HLA)³, observed as part of program GO-13364 (PI: Calzetti). Our multi-wavelength imaging data set included observations through the F336W (roughly corresponding to the Johnson–Cousins *U* band), F438W (*B*), F555W (*V*), and F814W (*I*) filters, which were pipeline-processed and calibrated using the standard HLA reduction software. They were already aligned to the same orientation and field of view, covering the inner galactic region (see Fig. 1). In this paper we assume a distance modulus of $(m - M)_0 = 30.48 \pm 0.25$ mag⁴, which corresponds to a distance of 13 Mpc. This results in a pixel scale of 2.4 pc pixel⁻¹. Since the circumnuclear starburst ring represents a small fraction of the full image, for convenience we cropped the ring-dominated area in the original four exposures to yield

a final, common science image of 585×585 pixels² (or 1400×1400 pc²), as shown in Fig. 1.

We used Kennicutt et al. (2009)’s calibration of the local SFR:

$$\text{SFR} (M_{\odot} \text{ yr}^{-1}) = 5.5 \times 10^{-42} [L(\text{H}\alpha)_{\text{obs}} + 0.011L(8 \mu\text{m})], \quad (2)$$

where $L(\text{H}\alpha)_{\text{obs}}$ is expressed in units of erg s^{-1} prior to any internal dust-attenuation correction, and $L(8 \mu\text{m})$ is the *Spitzer* $8 \mu\text{m}$ polycyclic aromatic hydrocarbon (PAH) emission-line luminosity, also in erg s^{-1} . This calibration was derived assuming a Kroupa initial mass function (IMF) with stellar masses in the range 0.1 – $100 M_{\odot}$ (Kroupa & Weidner 2003) and solar chemical abundance; Allard et al. (2006) and Sarzi et al. (2007) showed that circumnuclear regions of barred galaxies can be modeled well by adopting solar metallicity. $\text{H}\alpha$ emission is dominated by young massive stars and is commonly used as an instantaneous SFR indicator, tracing stars with lifetimes of ~ 3 – 10 Myr and masses greater than $40 M_{\odot}$ (e.g., Kennicutt et al. 2009; Hao et al. 2011). Since *HST* observations of the NGC 1512 circumnuclear ring in $\text{H}\alpha$ line emission are also available in the HLA, we additionally retrieved a narrow-band F658N ($\text{H}\alpha$) image (GO-6738; PI: Filippenko), observed with the WFPC2/Planetary Camera (PC). The PC chip has a pixel size of $\sim 0.05''$. The pixel scale of the $\text{H}\alpha$ image was resampled to match that of the WFC3 images ($\sim 0.04''$) and then aligned to the F555W frame, using standard IRAF/STSDAS⁵ routines. Observational information for all *HST* images used in this paper can be found in Table 1.

The aligned $\text{H}\alpha$ band is actually a combined emission line plus continuum image. To remove the underlying stellar continuum, we used the scaled F555W and F814W images on both the short- and long-wavelength sides of the F658N filter bandpass to linearly interpolate a continuum image at the reference $\text{H}\alpha$ wavelength. Since the WFC3 and WFPC2/PC detectors have almost the same PSF size, FWHM $\sim 0.07''$ (i.e., they have comparable spatial resolutions), we did not apply PSF matching. Next, the continuum image thus generated was subtracted from the F658N image, after converting both images from counts s^{-1} to the physical flux units of $\text{erg s}^{-1} \text{ cm}^{-2} \text{ \AA}^{-1}$ using the calibration parameter PHOTFLAM (i.e., the inverse sensitivity, contained in the image header), also listed in Table 1. This provides us with a reliable continuum subtraction without generating any conspicuous negative-flux regions, as shown in left-bottom panel of Fig. 1. As a consistency check, we compared our continuum-subtracted $\text{H}\alpha$ image to Fig. 1 of Maoz et al. (2001). The latter was generated based on their WFPC2/F547M and F814W images. We changed the display colors, inverted the associated color map, and adjusted the scale limits so as to match the appearance of Maoz et al.’s image as closely as possible. Although both images are indeed very similar, our new, higher-resolution image shows additional details in the form of dust lanes. This will, however,

³ <http://hla.stsci.edu/hlview.html>

⁴ This value, computed from values collected in the NASA Extragalactic Database (NED; <http://nedwww.ipac.caltech.edu/>), presents the geometric mean of 10 individual distance measurements from the literature.

⁵ The Image Reduction and Analysis Facility (IRAF) is distributed by the National Optical Astronomy Observatories, which are operated by the Association of Universities for Research in Astronomy, Inc., under cooperative agreement with the US National Science Foundation.

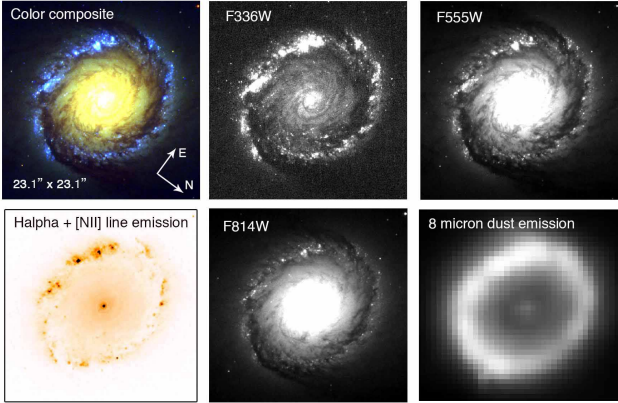


FIG. 1.— Top left: Color composite image of our target 585×585 pixels² nuclear ring area in NGC 1512, created by stacking images taken through the F336W, F555W, and F814W filters. The F336W filter, which traces young stellar populations, is shown in blue, while F555W and F814W are shown in green and red, respectively. The F555W and F814W images are shown in the middle and right-hand panels, respectively. Bottom: Continuum-subtracted $H\alpha$ /[NII] (left), F814W (middle), and continuum-subtracted $8 \mu\text{m}$ (right) images. All panels share the same orientation and field of view as indicated in the top left-hand panel.

not cause any problems in measuring the ring flux, since the faint continuum structure forms part of the background flux, which must be subtracted from the image (see below). We prefer to use the WFC3/F555W filter rather than WFC3/F547M, because the more recently installed WFC3 camera is characterized by better spatial resolution and improved efficiency. Moreover, the F555W image reaches fainter photoelectric limits and hence it shows more detailed structures compared with F547M. Note that our continuum-subtracted $H\alpha$ image includes adjacent [NII] lines redshifted to $\lambda\lambda 6568, 6604\text{\AA}$. We adopted a redshift of 0.0029 (Koribalski et al. 2004).

However, the possible effects of dust extinction in the $H\alpha$ filter significantly undermine its reliability for measuring the SFR. Dust particles in the interstellar medium absorb a fraction of the $H\alpha$ flux; the attenuated $H\alpha$ luminosity is subsequently re-radiated at infrared wavelengths. To more robustly estimate the dust-corrected SFRs, a better solution involves combining $H\alpha$ with infrared observations. We used the *Spitzer*/IRAC post-basic calibrated data (‘post-BCD’) images (3.6 and $8 \mu\text{m}$ bands, with a pixel scale of $0.6''$; see Table 1) taken from the *Spitzer* Heritage Archive and observed as part of the *Spitzer* Infrared Nearby Galaxies Survey (SINGS; Kennicutt et al. 2003). To derive the pure $8 \mu\text{m}$ PAH emission, needed as input in Eq. (2), we had to remove the stellar continuum contribution from the $8 \mu\text{m}$ image. Since the $3.6 \mu\text{m}$ band traces stellar mass in nearby galaxies (e.g., Elmegreen & Elmegreen 1984; Eskew et al. 2012; Meidt et al. 2012), a continuum-free PAH emission image at $8 \mu\text{m}$ can be obtained by subtracting a scaled $3.6 \mu\text{m}$ band image from the original $8 \mu\text{m}$ image, following the recipe of Helou et al. (2004) and employing a scale factor of 0.255. This approach results in highly accurate continuum-subtracted images, which has been widely demonstrated and used in the literature (e.g., Calzetti et al. 2007; Kennicutt et al. 2009; Zhou et al. 2015). The bottom right-hand panel of Fig. 1 shows the continuum-subtracted $8 \mu\text{m}$ image cropped

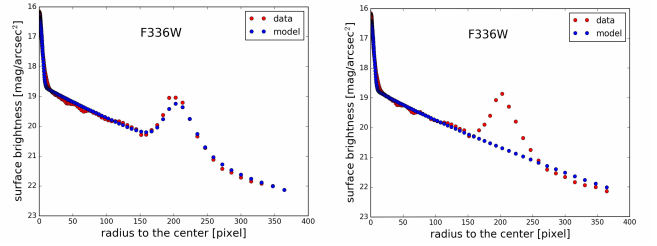


FIG. 2.— Radial profiles derived from the F336W image. Red dots represent the observed data and blue dots are for the best-fitting model. Left: Best-fitting model using three galactic components (i.e., background and nuclear ring). Right: Application of only a model of the background.

to focus on the inner ring area only.

3. MEASURING THE INTEGRATED RING LUMINOSITIES

To characterize the ring structure, we employed GALFIT to simultaneously fit the two-dimensional stellar light distributions of multiple galactic components using analytical functions. It generates a final model image based on the best-fitting structural parameters. The optimal solution for the model parameters is obtained using the iterative Levenberg–Marquardt algorithm (e.g., Bevington & Robinson 2003). Since the standard statistical uncertainties returned by GALFIT tend to underestimate the true uncertainties, we evaluated the goodness-of-fit based on both the χ^2 values given by GALFIT and visual inspection of the residual images.

3.1. *HST* image analysis

With regard to optical *HST* images, we have developed an improved approach to derive the total ring luminosity, based on inspection of the radial surface brightness profiles. To start with, we performed a test using the F336W image, which contains the most luminous nuclear ring component among our optical *HST* bands.

We plotted the radial surface brightness profile in the F336W image, shown as the red dotted line in the left-hand panel of Fig. 2. The presence of the nuclear ring introduces a prominent peak at radii between 118 and 250 pixels, corresponding to a radial range from $4.6''$ to $9.8''$. Therefore, we adopted this annulus to define the ring region in this paper. Based on the shape of the observed radial profile, we assume that our observed image consists of the host galaxy’s background contribution and a nuclear ring, and we intend to model all galactic components in the original image. The nuclear ring can be quantified by a truncation function, and the background contribution in the image can be fitted by adopting a mixture of Gaussian and Sérsic functions. This approach yields a good fit with minimal residuals. The truncation function is, in essence, a hyperbolic tangent function. In GALFIT these functions are commonly used to modify the light profiles of galactic components, such as Sérsic profiles, to produce ring-like structures (for a detailed description, see Peng et al. 2010).

To limit the degrees of freedom in the fits, we (only) fixed the center position; the other parameter were left as free parameters. We found a good match between the best-fitting model and the real data. The middle panel of Fig. 3 presents our best-fitting model based on the improved method, and the relevant radial profile is shown

TABLE 1
OBSERVATIONAL DETAILS OF THE FINAL NGC 1512 IMAGE DATA SET.

	Filter	Proposal ID/PI	Camera	Exposure time (s)	PHOTFLAM	Zmag
<i>HST</i>	F336W (<i>U</i>)	GO-13364/Calzetti	WFC3	1107	$1.3168305 \times 10^{-18}$	23.6012
	F438W (<i>B</i>)	GO-13364/Calzetti	WFC3	953	$6.91138715 \times 10^{-19}$	24.3011
	F555W (<i>V</i>)	GO-13364/Calzetti	WFC3	1131	1.876528×10^{-19}	25.7166
	F658N(H α)	GO-6738/Filippenko	WFPC2/PC	5200	$1.45442135 \times 10^{17}$	20.993
	F814W(<i>I</i>)	GO-13364/Calzetti	WFC3	977	$1.5304799 \times 10^{-19}$	25.9379
<i>Spitzer</i>	Band	Program ID/PI	Camera	Exposure time (s)	FLUXCONV	Zmag
	3.6 μ m	SINGS1-159/Kennicutt	IRAC	193	0.1069	18.8024
	8 μ m	SINGS1-159/Kennicutt	IRAC	176	0.2026	17.1984

Notes. Keyword PHOTFLAM is given in units of $\text{erg s}^{-1} \text{cm}^{-2} \text{\AA}^{-1}$. The instrumental magnitudes have been converted to the STMAG magnitude system by applying the photometric zero-points (Zmag), whose calibration relies on the PHOTFLAM and PHOTZPT keywords, i.e., $Z\text{mag} = -2.5 \log(\text{PHOTFLAM}) + \text{PHOTZPT}$ (where $\text{PHOTZPT} = -21.10$ for the ST magnitude scale). The *Spitzer* Zmags were taken directly from the image headers.

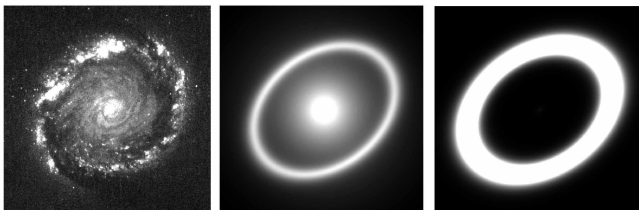


FIG. 3.— Left: Observed F336W image. Middle: Best-fitting three-component model for the F336W image. Right: Image of the individual truncation component based on the best-fitting model in the middle panel.

in the left-hand panel of Fig. 2 (blue dotted line; the red line represents the actual data). It is clear that a three-component model could entirely recover the observational profile with high accuracy. Using this method, the total ring luminosity can be derived by adding the flux in all pixels of the predefined ring region: see the right-hand panel of Fig. 3, which shows the truncation component (designed to model the nuclear ring). We determined $m_{\text{ring}}(U) = 14.83^{+0.05}_{-0.05}$ mag.

We also investigated how the use of different PSF images affected our fit results. We ran GALFIT using an empirical PSF, a theoretical PSF, and without any input PSF, respectively. We verified that the effect of changing the PSF is negligible, because the three conditions employed accurately reproduced the model image with the same structural parameters and the same resulting ring luminosity. This can be readily understood given the significant difference between the ring and the PSF sizes: the typical WFC3/UVIS stellar FWHM of $\sim 0.08''$ (e.g., Calzetti et al. 2015) is much smaller than the ring radius $\sim 8''$. To find the best fits faster, we opted to not provide the PSF when dealing with our *HST* images.

We subsequently applied our method to the other *HST* filters. The measured total ring magnitudes in the other filters in our data set are listed in Table 2. Note that no attempt was made to obtain a definitive model for the bulge. Our main goal was just to measure the proper, localized ring structure, with the remaining parts of the image together considered the image's (i.e., the ring's) background.

To determine the observed ring's H α luminosity, we applied our method to the continuum-subtracted H α + [NII] image produced in the previous section. We found $L(\text{H}\alpha + [\text{NII}]) = 5.61 \times 10^{39} \text{ erg s}^{-1}$, with a fractional uncertainty of $\sim 10\%$. This is very close to the luminosity ($6 \times 10^{39} \text{ erg s}^{-1}$) derived by Maoz et al. (2001),

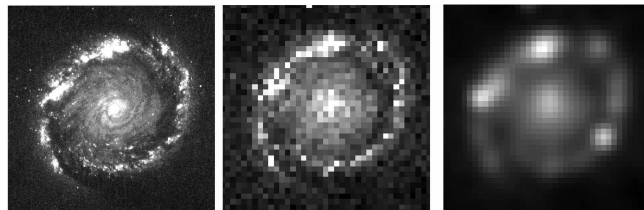


FIG. 4.— Left: Original F336W image. Middle: As the left-hand image, but for a pixel scale that has been degraded to that of the infrared image. Right: Final image after degradation of its pixel scale and Gaussian smoothing, so as to mimic the observed infrared data.

although those authors did not actually define a clear-cut ring region. Next, we corrected for the contributions of the [NII] lines using the theoretical [NII] flux line ratio (1/3; Osterbrock & Ferland 2006) and the observed [NII] λ 6584/H α flux line ratio of NGC 1512 obtained from Calzetti et al. (2007). $L([\text{NII}])$ was removed as a function of transmission efficiency of the F658N filter at the position of the lines. We obtained $L_{\text{obs}}(\text{H}\alpha) = 4.74 \times 10^{39} \text{ erg s}^{-1}$, which will be used to calculate the ring's SFR, together with $L(8 \mu\text{m})$, discussed in the next subsection.

3.2. *Spitzer* image analysis

A caveat regarding the *Spitzer*/IRAC image is that the IRAC image resolution for a typical PSF FWHM $\sim 2''$ is much lower than that of the *HST* PSF. As illustrated in the bottom right-hand panel of Fig. 1, such a resolution is comparable to the radius of the ring, and hence we cannot ascertain whether or not the measured ring luminosity would be affected by the lower *Spitzer* resolution. To clarify this issue, our strategy consisted of artificially degrading the *HST*/WFC3 F336W image to the resolution of *Spitzer*/IRAC so as to simulate the conditions pertaining to low resolution. We subsequently ran GALFIT on the degraded F336W image to verify whether we could recover the same result as that derived before image degradation. To construct the simulated image, we first changed its pixel size to that of *Spitzer* ($\sim 0.6''/\text{pixel}$), as shown in the middle panel of Fig. 4. It was then broadened by convolution with a Gaussian kernel to match the smoothness of the *Spitzer* image, as shown in the right-hand panel of Fig. 4. We found that the ring magnitude derived from our simulated image is $m_{\text{ring}}(U) = 14.83^{+0.19}_{-0.17}$ mag, which is in very good agreement with that obtained prior to image degradation, supporting the application of our method

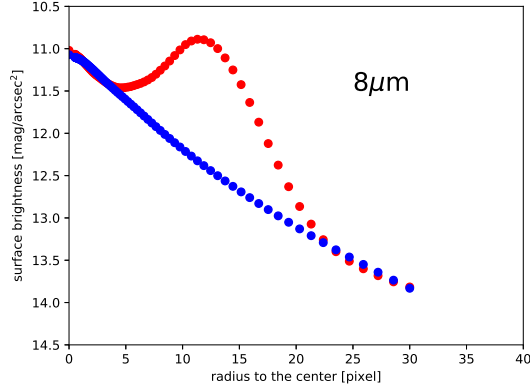


FIG. 5.— Radial profile of the ring in the *Spitzer* $8\ \mu\text{m}$ image. The red dotted line represents the actual data, while the blue line is the best-fitting background.

to *Spitzer* images.

We next applied our method to the continuum-subtracted *Spitzer* $8\ \mu\text{m}$ image, with the input PSF image artificially created by the STINYTIM package (Krist et al. 2005, which is a new version of TINYTIM developed specifically for *Spitzer* data). It is important to note that the ring is morphologically rather extended in the infrared compared with its extent in the optical images, but we chose the ring region according to that defined in the previous subsection to obtain its PAH emission-line luminosity, an essential parameter to determine the ring’s SFR. In essence, our standard ring region was defined on the basis of the *HST*/F336W image, which traces the young stellar population. The equation we used to determine the SFR is also sensitive to the age range (roughly from 3 Myr to 10 Myr).

The resulting luminosity is $L(8\ \mu\text{m}) = (8.857 \pm 0.6) \times 10^{41}\ \text{erg s}^{-1}$. Substituting $L(8\ \mu\text{m})$ and $L(\text{H}\alpha)_{\text{obs}}$ into Eq. (2), we derive an extinction-corrected $L(\text{H}\alpha)_{\text{corr}} = (1.445 \pm 0.17) \times 10^{40}\ \text{erg s}^{-1}$, which is within the estimated range of $\text{H}\alpha + [\text{NII}]$ luminosity given by Maoz et al. (2001), who provided an order-of-magnitude estimation in the range from $\sim 10^{40}$ – $10^{41}\ \text{erg s}^{-1}$. This indicates a total SFR of $0.08\ M_{\odot}\ \text{yr}^{-1}$ based on Eq. (2). The area of the ring is $0.879\ \text{kpc}^2$, so the SFR surface density (i.e., the star formation per unit area) is $\Sigma_{\text{SFR}} = 0.09\ M_{\odot}\ \text{yr}^{-1}\ \text{kpc}^{-2}$, which is about an order of magnitude higher than the disk-averaged SFR densities in normal galaxies (e.g., Kennicutt 1998).

For comparison, we also explored the performance of a simpler method to determine the ring flux. Here, we tried to obtain the best-fitting ring background profile. As before, the background can be modeled by Sérsic and Gaussian functions. However, the ring region was masked to prevent overestimation of the background before running the fit. The blue dotted line in the right-hand panel of Fig. 2 shows the best-fitting background in the F336W data, which matches the real background nicely. The total ring luminosity can be derived by subtracting the model from the data across the ring region, yielding $m_{\text{ring}}(U) = 14.76^{+0.13}_{-0.15}\ \text{mag}$. The associated uncertainties were estimated by considering both the fitting errors and the influence of different masking annulus radii

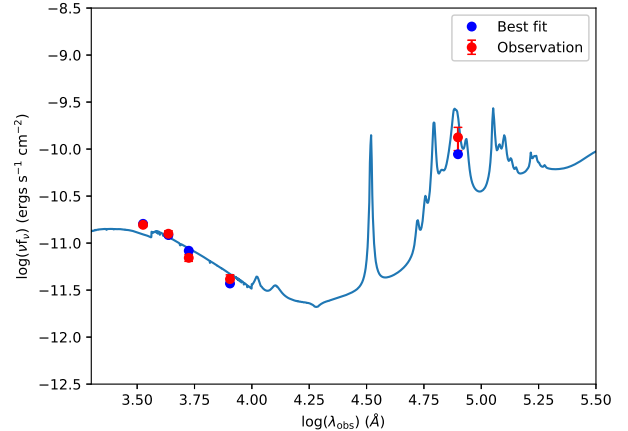


FIG. 6.— Spectral energy distribution. The observed broadband ring fluxes are shown as red dots, along with the photometry (blue dots) and the best-fitting model spectrum (blue line). Because of the relatively low resolution of *Spitzer*, the fit in the $8\ \mu\text{m}$ band has a larger uncertainty.

applied to the ring. This is, within the uncertainties, consistent with the value resulting from our more elaborate method: see Table 2 for comparison.

We note that the integrated ring luminosity returned by our improved method (see Section 3.1) is derived completely based on adequate model assumptions, including the use of a truncation function to model the ring, but for this simpler method the luminosity is directly derived from the ‘real’ image. The fact that our two different approaches reach the same conclusion for this particular image featuring a very bright ring component demonstrates the feasibility of our more elaborate method and the robustness of the results under such circumstances. The ring magnitude is a function of wavelength and age, however. The nuclear ring gradually becomes less prominent toward redder wavelengths, and it is almost undetectable in the radial profile of the F814W image, as shown in Fig. 1. Application of our simple method would hence lead to unreasonably large uncertainties. It is therefore only suitable for blue filters and/or very luminous rings.

Because of the remarkably luminous ring seen in our continuum-subtracted $8\ \mu\text{m}$, $\text{H}\alpha + [\text{NII}]$, and $8\ \mu\text{m}$ images, as evidenced in both Fig. 1 and Fig. 5, we proceeded to fit their backgrounds based on application of the simple model as well (see Fig. 5 for an example). We found that the resulting flux values and the SFR derived were consistent with those found using the more elaborate method: see Table 2. Table 2 also includes the best-fitting ring parameters (see below).

3.3. Spectral energy distribution modeling

We next modeled the observed SED using Flexible Stellar Population Synthesis models (FSPS; Conroy et al. 2009; Conroy & Gunn 2010) to derive the ring’s average age and total stellar mass. We did not correct for emission-line contamination to the broadband magnitudes, because this minor effect can be ignored. The stellar population synthesis model templates were internally generated over a grid of stellar population parameters, with the metallicity again fixed to the solar value. We assumed a Kroupa (2001) IMF, and

TABLE 2
PHOTOMETRY AND PHYSICAL PROPERTIES OF THE NGC 1512 RING

$H\alpha+[NII]$	F336W	F438W	F555W	F814W	$8\mu m$	continuum-subtracted $8\mu m$
13.93 ± 0.06	14.83 ± 0.05	15.23 ± 0.08	$16.12^{+0.12}_{-0.10}$	17.14 ± 0.17	5.58 ± 0.27	5.60 ± 0.28
$13.87^{+0.10}_{-0.09}$	$14.76^{+0.13}_{-0.15}$	—	—	—	5.66 ± 0.31	5.69 ± 0.31
	$\log(t \text{ yr}^{-1})$	$\log(M/M_{\odot})$	dust1	dust2		
Best-fitting parameters	$7.63^{+0.15}_{-0.31}$	7.1 ± 0.11	$1.06^{+0.68}_{-0.65}$	$0.57^{+0.22}_{-0.20}$		
$(M/L) \times L$	7.17	7.15	7.08	7.2	7.72	

Notes. We do not provide the photometric results from the simple method for redder optical filters, because of the intrinsically large uncertainties (see the text). The logarithmic mass estimates, based on the M/L s calculated, are also given as a function of filter/wavelength. **dust1** and **dust2** are dimensionless parameters.

left the age, mass, and dust parameters free in the fits. In FSPS models, the (dimensionless) dust parameters **dust1** and **dust2** describe the attenuation of young and old stellar light, respectively (for a detailed description, see Conroy et al. 2009), corresponding to $\hat{\tau}_1$ and $\hat{\tau}_2$ in Charlot & Fall (2000)’s prescription (their Eq. 5.8). The priors of our free parameters were $6.0 < \log(M/M_{\odot}) < 9.0$, $6.0 < \log(t/\text{yr}) < 10$, $0.1 < \text{dust1} < 2.0$, and $0.1 < \text{dust2} < 2.0$. For each parameter, a posterior probability distribution was constructed by employing Markov chain Monte Carlo methodology.

Figure 6 shows our best-fitting result; the photometry is represented by the blue dots, while the solid line is the model spectrum based on the best-fitting parameters. The best-fitting stellar mass is $\log(M/M_{\odot}) = 7.1 \pm 0.11$, and the error bars are the 16th and 84th percentiles of the model posteriors. This mass value corresponds to approximately 0.004% and 0.2% of the total dynamical and the HI masses of NGC 1512 (e.g., Koribalski & López-Sánchez 2009), respectively. To further examine the reliability of the derived mass, we calculated the mass-to-light ratio (M/L) based on the best-fitting parameters. The mass can then be estimated approximately by multiplying by our observed photometry. As shown in Table 2, we found that the derived masses based on the best-fitting M/L ratios are consistent within the 1σ error ranges in our four *HST* filters, with the $8\mu m$ band being the only outlier. This is mainly due to the larger observational uncertainty in that filter. This reflects the robustness of our mass determination. The best-fitting average age is $\log(t \text{ yr}^{-1}) = 7.63^{+0.15}_{-0.31}$, in agreement with the young-starburst characteristics of the ring. Given the present-day SFR derived above and the ring’s average age, the total stellar mass formed over its 40 Myr lifetime assuming a constant SFR, would amount to $\sim 3.8 \times 10^6 M_{\odot}$. This only accounts for approximately one-quarter of the best-fitting total ring mass. This insight thus demonstrates that the nuclear ring’s star-formation history is likely more complex. There is some evidence that the observed emission lines in the ring might be best modeled by adopting multiple starburst episodes of varying intensity rather than by a constant SFR (e.g., Allard et al. 2006; Sarzi et al. 2007).

Based on the publicly available optical *HST*/WFC3 and infrared *Spitzer*/IRAC images, we have presented an improved method (based on the GALFIT code) to derive the SED and SFR of the conspicuous nuclear ring in the barred spiral galaxy NGC 1512. The good agreement between the results from our improved method with that from a simple two-component method indicates that it is possible to accurately measure the integrated ring properties. We derived the SFR following the prescription given by Kennicutt et al. (2009). Based on Eq. (2), this offers a composite (multi-wavelength) $H\alpha+8\mu m$ -based SFR which is attenuation-corrected (composite methods provide more robust SFRs than any of the single-wavelength methods). We treated the contribution of the background intrinsic to the host galaxy more carefully, through modeling the light profile in the observed images. These two aspects represent the most important novel aspects of our study, since they enable us to obtain more realistic SFRs characterized by smaller uncertainties than those derived in previous studies.

All nuclear components of the galaxy in the image were modeled using analytical functions. To derive the ring’s current SFR, we constructed high-quality continuum-subtracted $H\alpha$ and $8\mu m$ images. The resulting SFR surface density (Σ_{SFR}) is $0.09 M_{\odot} \text{ yr}^{-1} \text{ kpc}^{-2}$. Our approach represents a significant improvement in measurement accuracy compared with previous efforts in the literature, which are often based on simple assumptions. Finally, we compared the observed ring’s SED with FSPS model SEDs to derive its physical properties, including its average age and total stellar mass. The NGC 1512 ring has a total stellar mass of $\sim 10^7 M_{\odot}$ and a young average age of around 40 Myr.

We have compiled a catalog of nuclear rings which have already been observed and are well resolved by both the *HST* (in at least four filters, ideal for further star cluster analysis) and *Spitzer* telescopes. In an extensive follow-up study, we are working on application of our improved method to a statistically carefully selected sample of nuclear rings. We will combine these results with the detected cluster populations to explore possible relationships between ring star-formation properties and those of the young cluster populations (e.g., cluster luminosity and mass functions, the cluster mass fraction, and cluster formation efficiencies). Our main objective in this paper was, therefore, to develop essential technical tools for our follow-up statistical study.

ACKNOWLEDGMENTS

We thank Hua Gao and Jinyi Shangguan for their generous help with technical issues and valuable discussions. This paper is based on observations made with the NASA/ESA *Hubble Space Telescope* and obtained from the *Hubble* Legacy Archive, which is a collaboration between the Space Telescope Science Institute (STScI/NASA), the Space Telescope European Coordinating Facility (ST-ECF/ESA), and the Canadian Astronomy Data Centre (CADC/NRC/CSA). This work also uses observations made with the *Spitzer Space Tele-*

scope, which is operated by the Jet Propulsion Laboratory, California Institute of Technology, under a contract with NASA. This research has also made use of NASA's Astrophysics Data System Abstract Service. We acknowledge research support from the National Natural Science Foundation of China through grants U1631102, 11373010, and 11633005 (C. M. and R. d. G.) and 11473002 and 11303008 (L. C. H.). L. C. H. also acknowledges support from the National Key Program for Science and Technology Research and Development, grant 2016YFA0400702.

REFERENCES

- Athanassoula, E. 1992, MNRAS, 259, 345
 Athanassoula, E., 1994, in Shlosman I., ed., Mass-Transfer Induced Activity in Galaxies. Cambridge Univ. Press, Cambridge, p. 143
 Allard, E. L., Knapen, J. H., Peletier, R. F., & Sarzi, M. 2006, MNRAS, 371, 1087
 Anders P., Fritze-v. Alvensleben U., 2003, A&A, 401, 1063
 Barth, A. J., Ho, L. C., Filippenko, A. V., & Sargent, W. L. W. 1995, AJ, 110, 1009
 Benedict, G. F., Howell, D. A., Jørgensen, I., Kenney, J. D. P., & Smith, B. J. 2002, AJ, 123, 1411
 Bevington, P. R., & Robinson, D. K. 2003, Data Reduction and Error Analysis for the Physical Sciences (3rd ed.; Boston: McGraw-Hill)
 Burbidge, E. M., & Burbidge, G. R. 1960, ApJ, 132, 30
 Buta, R., & Combes, F. 1996, FCPH, 17, 95
 Buta, R., & Crocker, D. A. 1993, AJ, 105, 1344
 Buta, R., Crocker D. A., Byrd, G. G., 1999, AJ, 118, 2071
 Buta, R., Treuthardt, P. M., Byrd, G. G., & Crocker, D. A. 2000, AJ, 120, 1289
 Byrd, G., Rautianen, P., Salo, H., Buta, R., & Crocker, D. A. 1994, AJ, 108, 476
 Calzetti D. et al., 2007, ApJ, 666, 870
 Calzetti, D., Lee, J. C., Sabbi, E., et al., 2015, AJ, 149, 51
 Charlot S., & Fall, S. M., 2000, ApJ, 539, 718
 Comerón, S., Knapen, J. H., Beckman, J. E., et al. 2010, MNRAS, 402, 2462
 Combes, F., 2001, in Aretxaga I., Kunth, D., Mújica, R., eds, Advanced Lectures on the Starburst-AGN Connection. World Scientific, Singapore, p. 223
 Conroy, C., & Gunn, J. E., 2010, ApJ, 712, 833
 Conroy, C., Gunn, J. E., White, M., 2009, ApJ, 699, 486
 de Grijs, R., & Anders, P., 2012, ApJ, 758, L22
 de Grijs, R., Ma, C., Jia, S. Y., Ho, L. C., & Anders, P., 2017, MNRAS, 465, 2820
 Elmegreen D. M., & Elmegreen B. G., 1984, ApJS, 54, 127
 Englmaier, P., & Shlosman, I. 2000, ApJ, 528, 677
 Eskew, M., Zaritsky, D., & Meidt, S., 2012, AJ, 143, 139
 Genzel, R., Weitzel, L., Tacconi-Garman, L. E., Blietz, M., Cameron, M., Krabbe, A., Lutz, D., & Sternberg, A. 1995, ApJ, 444, 129
 Hao, C.-N., Kennicutt, R. C., Johnson, B. D., et al. 2011, ApJ, 741, 124
 Helou, G., et al. 2004, ApJS, 154, 253
 Hsieh, P.-Y., Ho, P. T. P., Kohno, K., Hwang, C.-Y., & Matsushita, S. 2012, ApJ, 747, 90
 Hummel, E., van der Hulst, J.M., & Keel, W. C. 1987, A&A, 172, 32
 Kennicutt, R. C., Jr., 1983, ApJ, 272, 54
 Kennicutt R. C., Jr, 1998, ApJ, 498, 541
 Kennicutt, R. C. 1998, ARA&A, 36, 189
 Kennicutt, R. C., Jr et al., 2003, PASP, 115, 928
 Kennicutt, R. C., Hao, C.-N., Calzetti, D., et al. 2009, ApJ, 703, 1672
 Kennicutt R. C., & Evans N. J., 2012, ARA&A, 50, 531
 Kim, W.-T., Seo, W.-Y., & Kim, Y. 2012a, ApJ, 758, 14
 Kim, W.-T., Seo, W.-Y., Stone, J. M., Yoon, D., & Teuben, P. J. 2012b, ApJ, 747, 60
 Knapen, J. H., Beckman, J. E., Heller, C. H., Shlosman, I., & de Jong, R. S. 1995, ApJ, 454, 623
 Knapen, J. H., Mazzuca, L. M., Böker, T., et al. 2006, A&A, 448, 489
 Koribalski B. S., López-Sánchez A. R., 2009, MNRAS, 400, 1749
 Koribalski, B. S., Staveley-Smith, L., Kilborn, V. A., et al. 2004, AJ, 128, 16
 Kormendy, J., & Kennicutt, R. C., Jr. 2004, ARA&A, 42, 603
 Kroupa, P., & Weidner, C. 2003, ApJ, 598, 1076
 Krist, J.E., Ardila, D.R., Golimowski, D.A., et al., 2005, AJ, 129, 1008
 Li Z., Shen J., Kim W.-T., 2015, ApJ, 806, 150
 Maciejewski, W. 2004, MNRAS, 354, 892
 Maoz, D., Barth, A. J., Sternberg, A., et al. 1996, AJ, 111, 2248
 Maoz, D., Barth, A. J., Ho, L. C., Sternberg, A., & Filippenko, A. V. 2001, AJ, 121, 3048
 Mazzuca, L. M., Knapen, J. H., Veilleux, S., & Regan, M. W. 2008, ApJ, 174, 337
 Mazzuca, L. M., Sarzi M., Knapen, J. H., Veilleux, S., Swaters, R., 2006, ApJ, 649, 79
 Mazzuca, L. M., Swaters, R. A., Knapen, J. H., & Veilleux, S. 2011, ApJ, 739, 104
 Meidt S. E. et al., 2012, ApJ, 744, 17
 Osterbrock D. E., Ferland G. J., 2006, Astrophysics of Gaseous Nebulae and Active Galactic Nuclei, 2nd edn. University Science Books, Sausalito, CA
 Peng, C. Y., Ho, L. C., Impey, C. D., & Rix, H.-W. 2002, AJ, 124, 266
 Peng, C. Y., Ho, L. C., Impey, C. D., et al. 2010, AJ, 139, 2097
 Regan, M. W., & Teuben, P. 2003, ApJ, 582, 723
 Sandage, A. R. 1961, The Hubble Atlas of Galaxies (Washington, DC: Carnegie Institution of Washington)
 Sarzi, M., Allard, E. L., Knapen, J. H., & Mazzuca, L. M. 2007, MNRAS, 380, 949
 Schlegel, D. J., Finkbeiner, D. P., & Davis, M. 1998, ApJ, 500, 525
 Shlosman, I., Begelman, M. C., Frank J., 1990, Natur, 345, 679
 Sérsic J. L., 1968, Atlas de galaxias australes
 Sil'chenko, O. K., & Moiseev, A. V., 2006, AJ, 131, 1336
 van der Laan, T. P. R., Schinnerer, E., Emsellem, E., et al. 2013, A&A, 551, A81
 Weiner, B. J., Sellwood, J. A., & Williams, T. B. 2001, ApJ, 546, 931
 Wild, W., Harris, A. I., Eckart, A., Genzel, R., Graf, U. U., et al. 1992, A&A, 265, 44
 Willick, J. A., Courteau, S., Faber, S. M., et al. 1997, ApJS, 109, 333
 Zhou, Z.-M., Cao, C., & Wu, H. 2015, AJ, 149, 1